Eur. Phys. J. B (2019) 92: 32
https://doi.org/10.1140/epjb/e2019-90444-0

THE EUROPEAN PHYSICAL JOURNAL B

Regular Article

Spin-dependent transport in all-carbon multifunctional spintronic device

Xiaoxiao Han, Jingjuan Yang, Peipei Yuan, and Baoan Bian[a]

School of Science, Jiangnan University, Wuxi 214122, P.R. China

Received 7 July 2018 / Received in final form 14 November 2018
Published online 11 February 2019

Abstract. By using density functional theory and non-equilibrium Green's function method, we investigate the spin-dependent transport properties of an all-carbon spintronic device consisting of a perylene molecule linked to two symmetrical ferromagnetic zigzag-edge graphene nanoribbon (ZGNR) electrodes via carbon atomic chains, where the magnetization of ZGNR electrodes are modulated by applying an external magnetic field. The device exhibits spin filtering and negative differential resistance (NDR) effect in parallel spin configuration. Bipolar spin filtering, spin rectifying and NDR effect are revealed in antiparallel spin configuration. And there is a giant magnetoresistance effect between parallel and antiparallel spin configurations. We discuss these interesting transport mechanisms, and suggest that the proposed all-carbon device holds promise in high-performance multifunctional nanoelectronic devices.

1 Introduction

Single-molecule spintronic device will play an important role in the next generation of electronic systems due to its excellent performance [1–3]. Spintronic devices attract more attention, in which spin filtering [4], spin crossover [5], negative differential resistance (NDR) effect [6], giant magnetoresistance (GMR) effect [7] are found. These unique phenomena can improve quantum computation and data storage capability of nanoelectronic devices in the future. In recent years, the theoretical studies on single-molecule spintronic devices have been carried out [8–10]. Organic molecules play an active role in spintronic devices, because they hold weak spin-orbit interactions, weak hyperfine interactions, long spin-relaxation times and mechanical flexibility [11–13]. A number of multifunctional and high-performance spintronic devices based on organic molecular materials have been extensively studied. The spintronic devices based on the zinc methyl phenalenyl molecule exhibited spin filtering and rectifying effects [14]. There are high-efficiency GMR effect, spin filtering, spin rectifying and NDR effect in the planar four-coordinate Fe complex device [15]. These notable results showed that the spintronic devices based on organic molecular materials have broad prospects for multifunctional high-performance devices.

As we know, graphene nanoribbons (GNRs) have high carrier mobility and remarkable long spin-coherence time as well as distance, thus GNRs electrodes have been applied to the spintronic devices [16–18]. According to different edge of GNRs, there are two types of GNRs: armchair- and zigzag-edge GNRs (AGNRs and ZGNRs). AGNRs are nonmagnetic semiconductors [19,20]. Interestingly, researchers found that when ZGNRs edges are passivated by hydrogen atoms, it will hold the ground state with an antiferromagnetic (AFM) state. But the AFM state of ZGNRs has a great limitation in spintronics applications because its magnetic moment is zero. Previous studies have shown that the ZGNRs can be magnetized to a more stable ferromagnetic (FM) state by applying a transverse electrical field or a magnetic field [21,22], and this made ZGNRs well used as electrodes in spintronic devices. Recently, molecular device in which individual organic molecule is embedded in GNR electrodes has been successfully prepared and stably existed at room temperature, which indicates that molecular devices using GNR as electrodes are completely feasible and promising [23].

In addition, it is noteworthy that the stable carbon atomic chain (CAC) can be directly carved out from graphene sheet by using the electron irradiation [24]. Some interesting phenomena were found in several configurations of the CAC connected to the GNR leads. When CAC linked to ZGNR electrodes, a complete spin-polarization of the electron transmission was found in large energy ranges around the Fermi level [25]. It was found that the current–voltage characteristics of short CAC exhibit even-odd behavior, and NDR effect is found for both even and odd chain junctions [26]. High-performance spin diode of CAC between transverse symmetric ribbon electrodes was also reported [27]. Recently, organic molecular devices based on CACs have been extensively studied

[a] e-mail: baoanbian@163.com

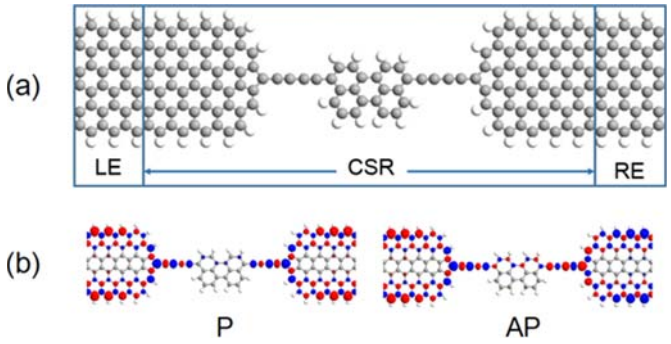

Fig. 1. (a) Schematic view of the all-carbon spintronic device. (b) Spin charge density difference for parallel (P) and antiparallel (AP) spin configurations at zero bias. The red and blue colors represent spin-up and spin-down, respectively.

theoretically. A phenyl ring is linked to the ZGNR electrodes through CACs, achieving perfect spin filtering and NDR effect. [28]. Similarly, a device consisting of chromium porphyrin-based molecule and CACs achieves the spin filtering with 100% spin polarization efficiency [29]. Perylene is a polycyclic aromatic hydrocarbon, and its derivatives have been investigated in organic optoelectronic materials both experimentally and theoretically [30–32]. Using scanning tunneling microscopy (STM), the researchers obtained high-resolution STM images of a perylene molecule adsorbed on Ag (110) surface [31]. The different adsorption modes of perylene on a titanium dioxide anatase (101) surface were investigated by density functional theory for efficient dye-sensitized solar cells [32]. In the present work, we study the spin-dependent transport properties of an all-carbon spintronic device consisting of a perylene molecule linked to two symmetrical ZGNR electrodes via CACs by employing the non-equilibrium Green's function method (NEGF) combined with the density functional theory (DFT). The results show that the all-carbon device can exhibit spin filtering (bipolar spin filtering), high-efficiency GMR effect, spin rectifying and NDR effect.

2 Model and method

The proposed all-carbon spintronic device is illustrated in Figure 1a. A perylene molecule is linked to the left and right infinite 6-ZGNR electrodes via CACs, and the number "6" is the width of the ZGNR along the direction perpendicular to the nanoribbon axis [33]. The device is separated into three regions: the left electrode (LE), the central scattering region (CSR), the right electrode (RE). The semi-infinite electrodes are modeled by a supercell with three repeated ZGNR unit cells along the transport direction, the CSR includes the perylene molecule, CACs, and four repeated ZGNR unit cells from each electrode to avoid the interaction between the electrodes and the central molecule. The enough vacuum layer (15 Å) is taken to eliminate interactions between neighboring periodic images. The edges of the two ZGNR electrodes are considered as FM state. The magnetization of the two electrodes can be modulated by applying an external magnetic field. In the calculations, we consider two kinds of spin orientation, parallel (P) spin configuration and antiparallel (AP) spin configuration.

The geometric optimization and spin-dependent transport calculations are performed by using the Atomistix Toolkit (ATK) package, which is based on NEGF and DFT [34,35]. The electron exchange-correlation is described by the generalized gradient approximation (GGA) with a Perdew–Burke–Ernzerhof (PBE) functional, and the valence electronic orbitals of all atoms are expanded in a single-ζ plus polarization (SZP) basis since it is good enough in our calculations [29,36]. The atomic positions in the CSR are fully relaxed until all atomic residual forces are smaller than 0.02 eV/Å. The k-point sampling is $1 \times 1 \times 100$, and the energy cutoff for grid integration is 150 Ry. The spin-dependent current through the device is calculated by the Landauer–Büttiker formula [37]:

$$I_\sigma(V_b) = \frac{e}{h} \int T_\sigma(E, V_b)[f_L(E - \mu_L) - f_R(E - \mu_R)]dE \tag{1}$$

where the σ is the spin index (spin-up or spin-down), $f_{L(R)} = 1/[1 + e^{(E-\mu_{L(R)})/k_B T}]$ is the Fermi-Dirac distribution function of energy E and the temperature T of the LE (RE). $\mu_{L(R)}$ denotes the electrochemical potential of the LE (RE) at the bias V_b, k_B is Boltzmann constant. $T_\sigma(E, V_b)$ is the spin-dependent transmission function of spin-up (spin-down):

$$T_\sigma(E, V_b) = \mathrm{Tr}[\Gamma^L_\sigma(E) G^r_\sigma(E) \Gamma^R_\sigma(E) G^a_\sigma(E)] \tag{2}$$

here, $G^{r(a)}_\sigma$ is the spin-dependent retarded (advanced) Green's function. $\Gamma^{L(R)}_\sigma = i(\sum^R_{L(R)}(E) - \sum^A_{L(R)}(E))$ is the coupling function between the LE (RE) and CSR, $\sum^R_{L(R)}(E)$ and $\sum^A_{L(R)}(E)$ are the self-energy matrices that consider the effect of the two electrodes.

3 Results and discussion

Figure 1b illustrates the spin charge density difference for P and AP spin configurations at zero bias. It can be seen that magnetism is mainly distributed on the edge atoms of ZGNR electrodes and CACs. Figures 2a and 2b depict the spin-dependent current–voltage (I–V) curves for P and AP spin configurations. In Figure 2a, the spin-up current (I_{up}) is much larger than the spin-down current (I_{dn}) at both positive and negative bias, and I_{dn} is almost zero. This indicates the spin-up transport channel is continuously open while the spin-down one is closed within the whole bias. Therefore, the all-carbon device in P spin configuration shows the spin filtering. Describing spin filtering, the bias-dependent spin filtering efficiency (SFE) is defined as SFE $= (I_{up} - I_{dn})/(I_{up} + I_{dn})$, and at zero bias, SFE $= (T_{up} - T_{dn})/(T_{up} + T_{dn})$, here T_{up} and T_{dn} indicate the transmission coefficients of spin-up and spin-down at the Fermi level, respectively. The SFE of P spin

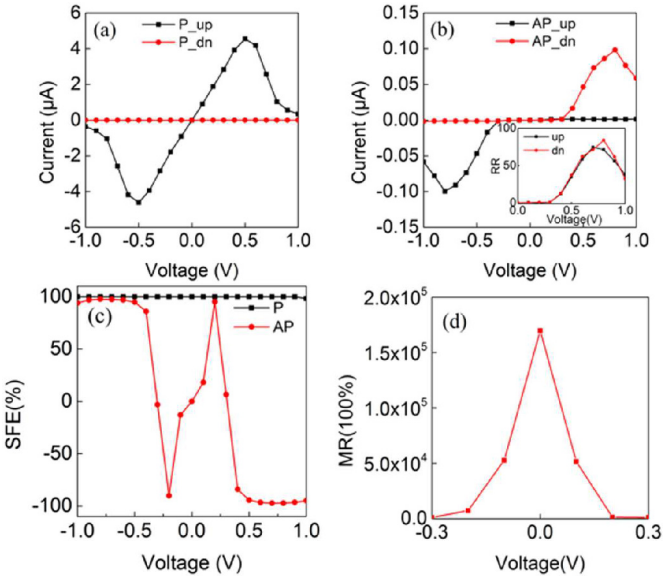

Fig. 2. (a) and (b) Spin-dependent current-voltage (I–V) curves for P and AP spin configurations. (c) Spin filtering efficiency (SFE) curves for P and AP spin configurations. (d) Magnetoresistance ratio (MR) of the GMR effect.

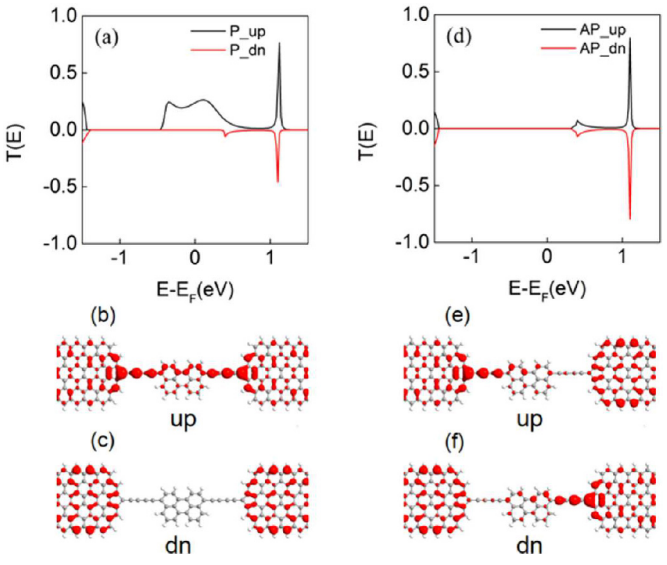

Fig. 3. The spin-dependent transmission peaks and the local density of states (LDOS) for (a–c) P spin configuration and (d–f) AP spin configuration at the Fermi level at zero bias.

configuration is nearly 100% as Figure 2c showed. In addition, it can be seen that when I_{up} exceed 0.5 (−0.5) V, I_{up} begins to decrease until 1.0 (−1.0) V. So I_{up} is suppressed at high bias, forming the NDR effect. Unlike P spin configuration, the current in AP spin configuration is embodied in unidirectional spin-dependent properties, i.e., I_{up} (I_{dn}) only appears when negative (positive) bias voltage exceeds −0.3 (0.3) V. This means that at positive bias, only spin-down channels are open, while at negative bias, only spin-up channels are open. Accordingly, the all-carbon device in AP spin configuration can display bipolar spin filtering and spin rectifying. The SFE reaches about 100% (−100%) when the bias value exceeds −0.3 (0.3) V. The spin-dependent rectification ratio (RR) for I_{up} (I_{dn}) is defined as RR = $|I_{up}(-V_b)/I_{up}(+V_b)|$ (RR = $|I_{dn}(+V_b)/I_{dn}(-V_b)|$), and the maximum RR value reaches about 75 (84) for I_{up} (I_{dn}). At small bias, the current of AP spin configuration is very small, even it can be negligible compared with P spin configuration, which reveals the GMR effect. The magnetoresistance ratio (MR) is defined as MR = $[(I_P - I_{AP})/I_{AP}] \times 100\%$, here I_P and I_{AP} are the total current of P and AP spin configurations, respectively. Particularly, at zero bias, we replace I_P (I_{AP}) with the transmission coefficients T_P (T_{AP}) and MR = $[(T_P - T_{AP})/T_{AP}] \times 100\%$. As illustrated in Figure 2d, the maximum MR reaches about 1.7×10^5 in the bias range of [−0.3 V, 0.3 V], which is larger than the results in previous studies [13,15,36]. In addition, I_{up} (I_{dn}) decreases at high bias (beyond −0.8 (0.8) V) causing the NDR effect. The NDR effect can be widely used in amplification [38], data storage [39], oscillators [40] and other applications in semiconductor devices.

To explain the unique spin-dependent transport characteristics in P and AP spin configurations, the spin-dependent transmission peaks and the local density of states (LDOS) at the Fermi level at zero bias are diagrammed in Figure 3. It is known that the electronic transmission of the device depends mainly on the transmission peak near the Fermi level. For P spin configuration, a large spin-up transmission peak occurs near the Fermi level, while there is no spin-down transmission peaks in Figure 3a, which is related to the distribution of the LDOS. In Figures 3b and 3c, the spin-up LDOS are distributed on the whole device, which provides a sufficient transport channel. While spin-down LDOS are only distributed on the electrodes, this leads to closed spin-down transport channel, thus there is no transmission peak near the Fermi level. For AP spin configuration in Figure 3d, spin-up and spin-down transmission peaks have similar characteristics, there is a small transmission peak far away from the Fermi level. The spin-up and spin-down LDOS are mainly localized on the two electrodes and one side of CACs shown in Figures 3e and 3f, therefore, the spin-up and spin-down transport are suppressed near the Fermi level.

To further explain the transport properties at finite bias, the spin-up and spin-down transmission spectra at different bias for P ([0 V, 1.0 V]) and AP ([0 V, 1.0 V] and [0 V, −1.0 V]) spin configurations are displayed in Figure 4. For P spin configuration in Figure 4a, the integral area of spin-up transmission peak gradually increases at the bias from 0 to 0.5 V. After 0.5 V, the peak within the bias window decreases and the integral area begins to decrease, then the NDR effect occurs. The variation of the spin-up transmission peak is consistent with the current trend of I_{up} in Figure 2a, i.e., I_{up} firstly increases and then gradually decreases within the bias voltage of [0 V, 1.0 V]. In Figure 4b, compared with spin-up transmission peak, there is almost no spin-down transmission peak within the bias window. Therefore, the integral area of spin-up is larger than the spin-down one, and this device can be regarded as a perfect filter in P spin configuration.

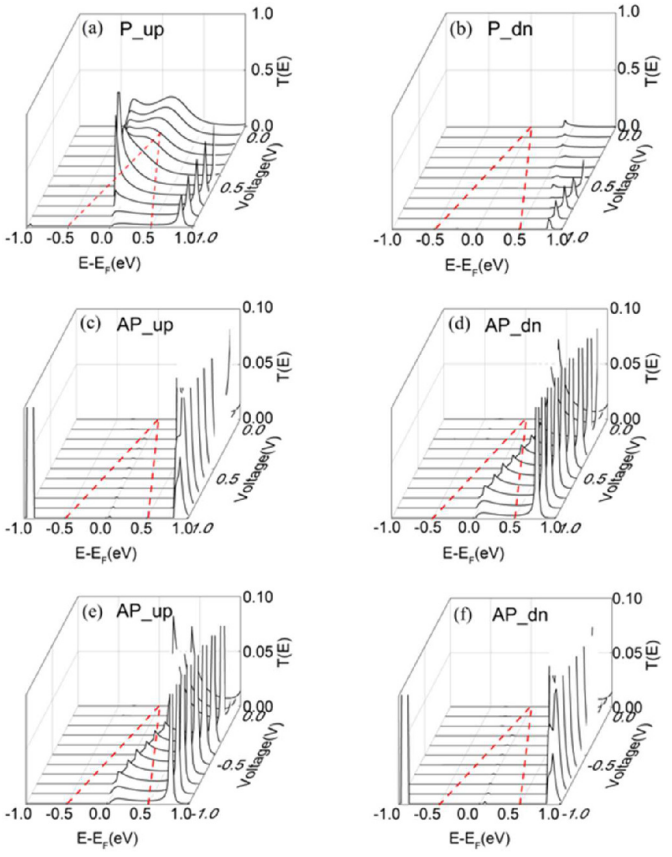

Fig. 4. (a) and (b) Spin-up and spin-down transmission spectra for P spin configuration within the bias range of [0 V, 1.0 V], (c) and (d) spin-up and spin-down transmission spectra for AP spin configuration within the bias range of [0 V, 1.0 V], (e) and (f) spin-up and spin-down transmission spectra for AP spin configuration within the bias range of [0 V, −1 V]. The region between two dashed red lines indicates the bias window.

For AP spin configuration, from Figures 4c to 4f, one can see that the spin-up transmission peaks appear at negative bias, and the spin-down transmission peaks appear at positive bias. This indicates that spin-up electrons can pass through the device at negative bias, and spin-down electrons can pass through the device at positive bias. When the bias exceeds −0.8 (0.8) V, I_{up} (I_{dn}) transmission peak integration area gradually decreases, resulting in NDR effect. It can be seen that there is no spin-up and spin-down transmission peaks within the bias window at small bias for AP spin configuration, as a result, there is almost no spin-dependent current at the small bias range, and the total current of AP spin configuration is less than that of P spin configuration. Consequently, the GMR effect appears when the device switches between P and AP spin configurations at small bias.

The electronic transport properties can be further explained by the band structures of both left and right electrodes plotted in Figure 5, position of molecular orbitals in Figure 5 and the corresponding molecular projected self-consistent Hamiltonian (MPSH) eigenstates shown in Figure 6. For P spin configuration, there are three spin-up molecular orbitals 314–316 and three

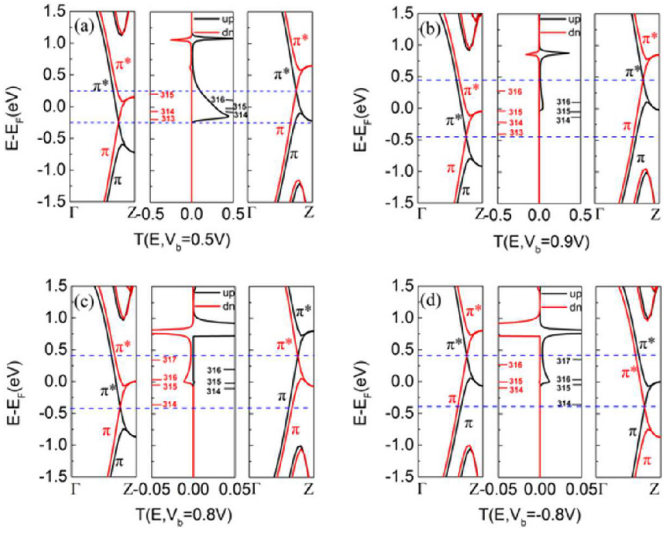

Fig. 5. Spin-dependent band structures for LE (left panels), RE (right panels), and transmission peaks (middle panels) at different bias. (a) and (b) Correspond to P spin configuration at 0.5 V and 0.9 V, respectively. (c) and (d) Correspond to AP spin configuration at 0.8 V and −0.8 V, respectively. The region between the two dotted blue lines indicate the bias window. The black and red short lines indicate the molecular orbitals position of spin-up and spin-down, respectively.

spin-down molecular orbitals 313–315 within the bias window at 0.5 V in Figure 5a. The spin-down molecular orbital 315 is located in the overlap area between π^* subband of LE and π subband of RE. The isosurface plots of bloch wave function of π^* (π) subband has even (odd) parity under the σ mirror operation in Figure 7, and electrons between π^* and π subbands are forbidden to transmit [41,42]. This indicates that the spin-down molecular orbital 315 has no contribution to transport. At 0.5 V, the spin-up MPSH eigenstates of molecular orbitals 314 and 316 are delocalized on the whole device, the spin-down molecular orbitals 313 and 314 are localized. Thus, there are spin-up transport channels, and spin-down transport channels are almost closed, the observed spin-up transmission peak and disappeared spin-down transmission peak result in spin filtering. As the positive bias continues to increase, subbands will continuously move down and up for LE and RE, respectively. At 0.9 V, there is only one spin-up molecular orbital 316 in the overlap area of symmetric subbands (π^* to π^*) in LE and RE shown in Figure 5b. The spin-up MPSH eigenstates of molecular orbital 316 is localized on RE, resulting in smaller transmission peak, thus the NDR effect is observed. The MPSH eigenstates of spin-down molecular orbitals 313 and 314 are localized, being far from the Fermi level, so the spin-down transport channel is still almost closed and no transmission peak occurs. For AP spin configuration, in Figures 5c and 5d, at positive bias, subbands of LE (RE) move down (up). While at negative bias, subbands of LE (RE) move up (down). At 0.8 V, there are three (four) spin-up (spin-down) molecular orbitals within the bias window. But all spin-up molecular orbitals do not contribute to the electronic transport due to the asymmetry

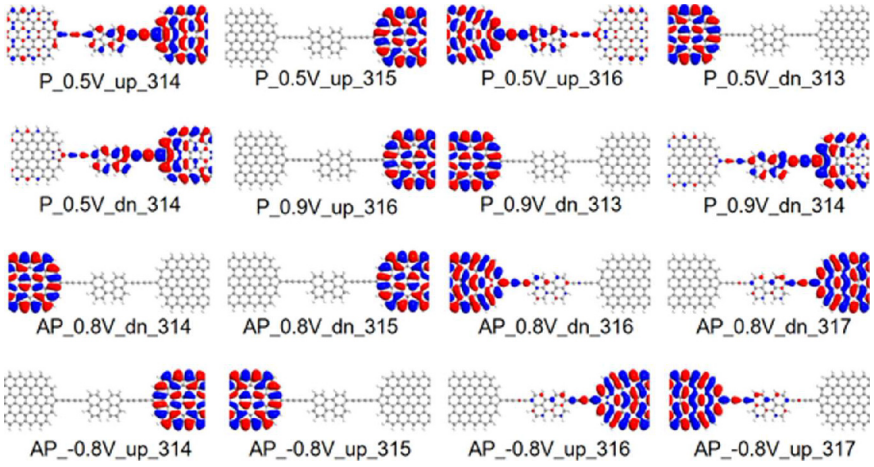

Fig. 6. Spatial distribution of the spin-dependent MPSH eigenstates of molecular orbitals within the bias window for P and AP spin configurations. In particular, those molecular orbitals that have no contribution to electronic transport are not shown here.

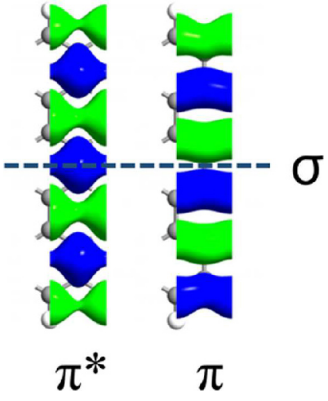

Fig. 7. Isosurface plots of Bloch wave functions of π^* and π subbands at the Fermi level of ZGNR.

of LE and RE subbands. As plotted in Figure 6, even if the spin-down MPSH eigenstates of molecular orbital 314 (315) is localized on LE (RE), the unconspicuous delocalization of the spin-down MPSH eigenstates of molecular orbitals 316 and 317 can provide weak transport channel. This leads to a smaller spin-down transmission peak at 0.8 V. The position of molecular orbitals in Figure 5d and MPSH eigenstates in Figure 6 indicate that there is a weak spin-up transport channel and a closed spin-down transport channel at −0.8 V, and only spin-up transmission peak appears. Consequently, there is only spin-down transmission peaks at positive bias, and only spin-up transmission peaks at negative bias, resulting in bipolar spin filtering and spin rectifying.

4 Conclusion

We investigate the spin-dependent transport properties of an all-carbon spintronic device consisting of a perylene molecule linked to two symmetrical ferromagnetic ZGNR electrodes by using the DFT and NEGF methods. The proposed device exhibits spin filtering and NDR effect for both P and AP spin configurations, spin rectifying for AP spin configuration. And there is a GMR effect between P and AP spin configurations. The maximum magnetoresistance ratio reaches about 1.7×10^5. The displayed transport properties were explained by the spin-dependent transmission spectra, LDOS, band structures, molecular orbitals and MPSH eigenstates. Theoretical investigations presented herein provide further understanding of the transport mechanism of spintronic devices, and these results also provide guidance for the design of new multifunctional and high-performance nanoelectronic devices.

This work is supported by the Fundamental Research Funds for the Central Universities under Grant Nos. JUSRP51628B and JUSRP51716A, and Postgraduate Research & Practice Innovation Program of Jiangsu Province under Grant No. SJCX17_0497.

Author contribution statement

In this work, Baoan Bian proposed the idea, Xiaoxiao Han performed the calculation, analyzed calculated results and wrote the manuscript. Jingjuan Yang and Peipei Yuan assisted with discussion of results.

References

1. J. Li, Z.H. Zhang, M. Qiu, C. Yuan, X.Q. Deng, Z.Q. Fan, G.P. Tang, B. Liang, Carbon **80**, 575 (2014)
2. A. Staykov, M. Watanabe, T. Ishihara, K. Yoshizawa, J. Phys. Chem. C **118**, 27539 (2014)
3. G.J. Simpson, S.W.L. Hogan, M. Caffio, C.J. Adams, H. Früchtl, T.V. Mourik, R. Schaub, Nano Lett. **14**, 634 (2014)
4. H. Hao, X.H. Zheng, Z.X. Dai, Z. Zeng, Appl. Phys. Lett. **96**, 192112 (2010)
5. H. Hao, X.H. Zheng, L.L. Song, R.N. Wang, Z. Zeng, Phys. Rev. Lett. **108**, 017202 (2012)
6. J. Huang, W.Y. Wang, Q.X. Li, J.L. Yang, J. Chem. Phys. **140**, 164703 (2014)

7. S. Schmaus, A. Bagrets, Y. Nahas, T.K. Yamada, A. Bork, M. Bowen, E. Beaurepaire, F. Evers, W. Wulfhekel, Nat. Nanotechnol. **6**, 185 (2011)
8. Z.Q. Fan, Z.H. Zhang, M. Qiu, X.Q. Deng, G.P. Tang, Appl. Phys. Lett. **101**, 073104 (2012)
9. X.J. Zhang, M.Q. Long, K.Q. Chen, Z. Shuai, Q. Wan, B.S. Zou, Y. Zhang, Appl. Phys. Lett. **94**, 073503 (2009)
10. X.B. Li, H. Gao, H.Q. Wan, H.L. Li, G.H. Zhou, Chem. Phys. Lett. **610**, 298 (2014)
11. J.M. Kikkawa, D.D. Awschalom, Nature (London) **397**, 139 (1999)
12. S. Sanvito, J. Mater. Chem. **17**, 4455 (2007)
13. P. Zhao, D.S. Liu, G. Chen, Org. Electr. **36**, 160 (2016)
14. C.M. Tan, Y.H. Zhou, C.Y. Chen, J.F. Yu, K.Q. Chen, Org. Electr. **28**, 244 (2016)
15. P. Zhao, Q.H. Wu, D.S. Liu, G. Chen, J. Chem. Phys. **140**, 044311 (2014)
16. O.V. Yazyev, M.I. Katsnelson, Phys. Rev. Lett. **100**, 047209 (2008)
17. G. Cantele, Y.S. Lee, D. Ninno, N. Marzari, Nano. Lett. **9**, 3425 (2009)
18. W. Han, R.K. Kawakami, Phys. Rev. Lett. **107**, 047207 (2011)
19. F. Muñoz-Rojas, J. Fernández-Rossier, J.J. Palacios, Phys. Rev. Lett. **102**, 136810 (2009)
20. Y.W. Son, M.L. Cohen, S.G. Louie, Phys. Rev. Lett. **97**, 216803 (2006)
21. Y.W. Son, M.L. Cohen, S.G. Louie, Nature **444**, 347 (2006)
22. W.Y. Kim, K.S. Kim, Nat. Nanotechnol. **3**, 408 (2008)
23. F. Prins, A. Barreiro, J.W. Ruitenberg, J.S. Seldenthuis, N. Aliaga-Alcalde, L.M.K. Vandersypen, H.S.J. Zant, Nano Lett. **11**, 4607 (2011)
24. C.H. Jin, H.P. Lan, L.M. Peng, K. Suenaga, S. Lijima, Phys. Rev. Lett. **102**, 205501 (2009)
25. J.A. Fürst, M. Brandbyge, A.P. Jauho, Europhys. Lett. **91**, 37002 (2010)
26. K.H. Khoo, J.B. Neaton, Y.W. Son, M.L. Cohen, S.G. Louie, Nano Lett. **8**, 2900 (2008)
27. Y.J. Dong, X.F. Wang, S.W. Yang, X.M. Wu, Sci. Rep. **4**, 6157 (2014)
28. H.Q. Wan, B.H. Zhou, X.G. Chen, C.Q. Sun, G.H. Zhou, J. Phys. Chem. C **116**, 2570 (2012)
29. T. Chen, L.L. Wang, X.F. Li, K.W. Luo, L. Xu, Q. Li, X.H. Zhang, M.Q. Long, RSC Adv. **4**, 60376 (2014)
30. C. Wagner, N. Fournier, F.S. Tautz, R. Temirov, Phys. Rev. Lett. **109**, 076102 (2012)
31. Z.T. Deng, H. Lin, W. Ji, L. Gao, X. Lin, Z.H. Cheng, X.B. He, J.L. Lu, D.X. Shi, W.A. Hofer, H.J. Gao, Phys. Rev. Lett. **96**, 156102 (2006)
32. S. Ikäläinen, K. Laasonen, Phys. Chem. Chem. Phys. **15**, 11673 (2013)
33. M. Fujita, K. Wakabayashi, K. Nakada, K. Kusakabe, J. Phys. Soc. Jpn. **65**, 1920 (1996)
34. M. Brandbyge, J.L. Mozos, P. Ordejon, J. Taylor, K. Stokbro, Phys. Rev. B **65**, 165401 (2002)
35. J. Taylor, H. Guo, J. Wang, Phys. Rev. B **63**, 245407 (2001)
36. P. Zhao, Q.H. Wu, H.Y. Liu, D.S. Liu, G. Chen, J. Mater. Chem. C **2**, 6648 (2014)
37. M. Büttiker, R. Landauer, Phys. Rev. B **31**, 6207 (1985)
38. M.G. Zeng, L. Shen, M. Zhou, C. Zhang, Y.P. Feng, Phys. Rev. B **83**, 115427 (2011)
39. Z.S. Su, M.K. Fung, C.S. Lee, W.L. Li, S.T. Lee, Appl. Phys. Lett. **93**, 083301 (2008)
40. E. Alekseev, D. Pavlidis, Solid-State Electr. **44**, 941 (2000)
41. Z.Y. Li, H.Y. Qian, J. Wu, B.L. Gu, W.H. Duan, Phys. Rev. Lett. **100**, 206802 (2008)
42. Z.F. Wang, Q.X. Li, Q.W. Shi, X.P. Wang, J.L. Yang, J.G. Hou, J. Chen, Appl. Phys. Lett. **92**, 133114 (2008)